Spin-texture driven reconfigurable magnonics in chains of connected $Ni_{80}Fe_{20}$ submicron dots

Amrit Kumar Mondal,[1] Chandrima Banerjee,[1] Arundhati Adhikari,[1] Avinash Kumar Chaurasiya,[1] Samiran Choudhury,[1] Jaivardhan Sinha,[1] Saswati Barman,[2] and Anjan Barman[1,*]

[1]*Department of Condensed Matter Physics and Material Sciences, S. N. Bose National Centre for Basic Sciences, Block JD, Sector III, Salt Lake, Kolkata 700106, India*

[2]*Institute of Engineering and Management, Sector V, Salt Lake, Kolkata 700 091, India*

(Received 8 January 2020; revised manuscript received 5 May 2020; accepted 28 May 2020; published 22 June 2020)

Topological magnonics has attracted intense interest for application in energy efficient computational devices. Here, we show reconfigurable magnonic band structure and band gap by a bias-field controlled spin texture in chains of connected $Ni_{80}Fe_{20}$ submicron dots. Particularly for an identical field value, we achieve both "*S*" and shifted-core vortex states based on magnetic history leading to a drastic change in magnonic band structure. A first-order phase transition from the saturation to vortex state drives this change, as opposed to a continuous change from the saturation to *S* state.

DOI: 10.1103/PhysRevB.101.224426

I. INTRODUCTION

Modern charge-based circuits consist of a large number of transistors fabricated as integrated chips with metallic interconnectors. With ever-increasing density of storage, memory, and processor units the technology faces huge challenges of thermal runaway [1] and the thermal management is proposed to be done more efficiently by spin-based devices. Consequently, research fields like spintronics [2,3], magnonics [4,5], spin-orbitronics [6], and magnon spintronics [7] have emerged rapidly during last few decades. In these fields, the charge current is replaced by various alternatives such as spin polarized current, pure spin current, and magnon current, to name a few. Magnonics use spin waves (SWs) as information carriers through a periodically patterned magnetic media, popularly known as magnonic crystal (MC). It deals with the excitation, propagation, and detection of magnons and its properties such as magnonic band structures, band gap, spatial mode profiles, etc. SWs have much smaller propagation velocity than that of the electromagnetic (EM) waves at the same frequency and hence, several order shorter wavelength (micro- to nanometer scale) than its EM-wave counterpart. Thus, magnonics fit perfectly with nanotechnology, leading towards on-chip data transfer and processing. The SW properties of MCs can be efficiently tailored by its geometric parameters such as shape [8], size [9], lattice constant [10], lattice symmetry [11], material [12], and external magnetic field, and reconfigurable magnonic band structure [13] can be obtained.

During the last decade coupled arrays of ferromagnetic nanodots have been studied in great detail [14–19]. Among them coupled chains of nanodots have attracted significant interest due to their inherently large shape anisotropy aiding efficient transfer of energy, while retaining its large tunability as opposed to a plain nanowire or nanostripe structure. Consequently, linear arrays of nanomagnets have been used to design magnetic logic architecture [18,19]. Furthermore, linear arrays of magnetic nanodisks containing vortex states have been shown to transfer excitation energy in terms of vortex core gyration aided by the SW [14,16] and its experimental demonstration [15,20] leading towards magnetic vortex-based logic operation [20] and proposed transistor operation [21]. Tunability of magnetic configurational anisotropy in differently ordered chains of elliptical nanomagnets have been demonstrated [22]. Recently, linear arrays of shaped nanomagnets have been used for reconfigurable waveguide design to transmit and locally manipulate SWs without the need for any external bias field after initialization [23]. More recently, strongly overlapped nanomagnets forming pseudo-one-dimensional magnonic crystals have shown reconfigurable magnonic band structure by slight variation of the bias field orientation [13]. However, the role of magnetic history dependent tunable spin texture on the SW propagation in a chain of nanomagnets has not been explored in the literature.

Here, we have investigated the SW dispersion by Brillouin light scattering (BLS) in chains of connected nanomagnets, where each nanomagnet with 30 nm thickness has a rounded rectangular shape with 780 nm × 540 nm lateral dimensions having a 230-nm radius of curvature of the rounded ends and they are all tilted at about 29° from the chain axis. By changing the magnetic-field history the spin texture is interchanged between magnetic leaf, "S," and vortex state and the ensuing magnonic band structure, including band gap, is reconfigured. A bifurcation [24–26] of magnetic state at an identical magnetic field is observed leading towards a remarkable change in the magnon dispersion, including the band gap and group velocity. The observations are important for designing nanomagnet-based bias-field reconfigurable and energy efficient magnon waveguides.

II. EXPERIMENTAL AND THEORETICAL METHODS

A $72 \times 72\,\mu m^2$ array of 30-nm-thick polycrystalline $Ni_{80}Fe_{20}$ (permalloy: Py hereafter) dots with geometry as

*Corresponding author: abarman@bose.res.in

described above has been fabricated in a square lattice symmetry onto a thermally oxidized silicon (001)/silicon oxide (Si/SiO_2) substrate using a combination of electron-beam lithography and electron-beam evaporation. The substrate is spin coated with bilayer polymethyl methacrylate (495 and 950 K) positive-tone *e*-beam resist. The beam current used during electron-beam lithography is 5.4 pA for a line dose of 1.5 nC/cm. The connected dot pattern is defined after development of the electron-beam exposed resist in methyl isobutyl ketone (MIBK) and isopropyl alcohol (IPA) (MIBK: IPA, 1:3) solution. Thereafter, 30-nm-thick Py is deposited at a deposition rate of 0.2 Å/S using electron-beam evaporation at a base pressure of 30 nTorr. A 2-nm-thick SiO_2 protective layer has been deposited on top of Py using rf sputtering (base pressure = 0.2 μTorr, Ar pressure = 5 mTorr, deposition rate = 0.3 Å/S, rf power = 60 W) to protect the sample from degradation. Subsequently, liftoff is done in acetone using ultrasonic agitation to obtain the connected dots. The surface topography of the sample is determined by scanning electron microscopy (SEM) and atomic force microscopy (AFM). The static magnetic configuration of the sample is imaged by magnetic force microscopy (MFM). The SW dispersion relation of the sample is measured by BLS spectroscopy in the conventional back-scattering geometry. The output of a single mode CW solid-state laser of wavelength (λ) of 532 nm with power of about 60 mW is made incident on the sample. The wave vector (k) associated with the SW has been calculated using the relation $\boldsymbol{k} = 2\boldsymbol{k}_{\rm in}\ \sin\theta = \frac{4\pi}{\lambda}\sin\theta$, where θ is the angle of incidence in the backscattered geometry and $k_{\rm in}$ represents the wave vector of the incident laser beam. In our experiment, we have probed k up to 8.2 rad/μm along the Γ-Y symmetry axis, i.e., up to the second Brillouin zone (BZ).

We have theoretically calculated SW dispersion [i.e., frequency (f) versus wave-vector (k) diagram] and spatial profile of the SW modes using plane wave method (PWM) [27]. For simplicity in this calculation, we have considered elliptical Py nanodots. The dynamics of magnetization [$M(r,t)$] for the MC in Fig. 1(a) is described by

$$\frac{\partial \boldsymbol{M}(r,t)}{\partial t} = -\gamma\mu_0 \boldsymbol{M}(\boldsymbol{r},t) \times \boldsymbol{H}_{\rm eff}(\boldsymbol{r},t). \tag{1}$$

Here, $\boldsymbol{H}_{\rm eff}(\boldsymbol{r},t)$ is the effective magnetic field, i.e.,

$$\boldsymbol{H}_{\rm eff}(\boldsymbol{r},t) = \boldsymbol{H} + \boldsymbol{H}_d + \boldsymbol{H}_{\rm ex}, \tag{2}$$

where $\boldsymbol{H}_d$ is the total demagnetizing field, which can be written as

$$\boldsymbol{H}_d = \boldsymbol{H}_d(r) + \boldsymbol{h}_d(r)e^{i2\pi\nu t}, \tag{3}$$

where $\boldsymbol{H}_d(\mathbf{r})$ and $\boldsymbol{h}_d$ are the static and dynamic components of the dipolar field, which satisfy magnetostatic Maxwell's equations. $\boldsymbol{H}$ and $\boldsymbol{H}_{\rm ex}$ are the applied magnetic field and exchange field, respectively, where $\boldsymbol{H}_{ex} = [\nabla \cdot l_{\rm ex}^2(\boldsymbol{r})\nabla]m(\boldsymbol{r},t)$, $l_{\rm ex}(\boldsymbol{r}) = \sqrt{\frac{2A(\boldsymbol{r})}{\mu_0 M_s^2(\boldsymbol{r})}}$ is the exchange length and $A(r)$ is the exchange stiffness constant. In the linear approximation, the component of the magnetization vector $\boldsymbol{M}_s(\boldsymbol{r})$ parallel to the static magnetic field (i.e., z axis in our case) is constant in time, and its magnitude is much greater than that of the perpendicular component $m(\boldsymbol{r},t)$, so that

$$\boldsymbol{M}(\boldsymbol{r},t) = \boldsymbol{M}_s(\boldsymbol{r})\hat{z} + \boldsymbol{m}(\boldsymbol{r},t). \tag{4}$$

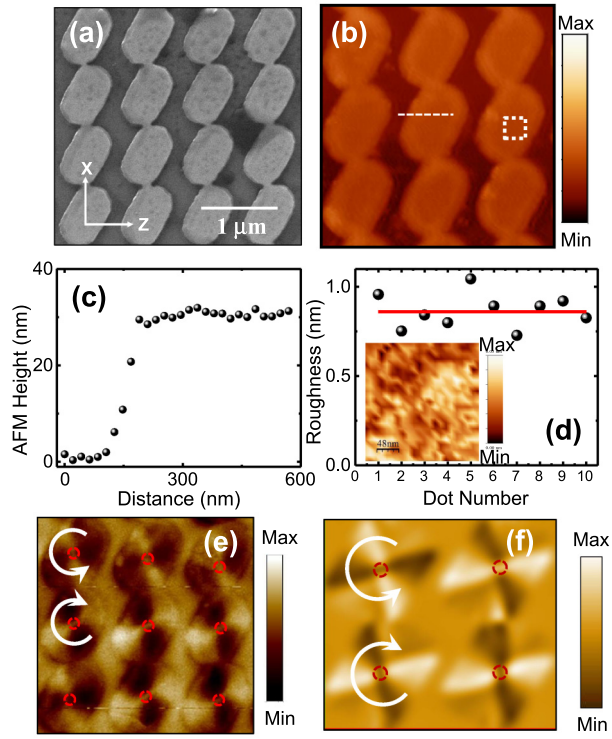

FIG. 1. (a) Scanning electron microscope (SEM) and (b) atomic force microscope (AFM) image of the sample. (c) Height of nanodot obtained from the AFM image along the dotted line in (b). (d) Roughness of various dots in the sample along with a high-resolution image taken from the dotted box in (b) is shown in the inset. (e) Experimental and (f) simulated magnetic force microscope (MFM) image of the sample in the AC demagnetized state. The arc arrows represent chirality of vortex found from the simulation.

To get the solution of the Landau-Lifshitz (LL) equation, we use Bloch's theorem with lattice constant a, so that $\boldsymbol{m}(\mathbf{r}) = \sum_{\boldsymbol{G}} m_k(\boldsymbol{G})e^{i(k+\boldsymbol{G})\cdot r}$, where wave vector $\boldsymbol{k} = (k_x, k_z)$ is in the first BZ, and $\boldsymbol{G} = (\boldsymbol{G}_x, \boldsymbol{G}_z) = \frac{2\pi}{a}(n_x, n_z)$ denotes the reciprocal-lattice vector of the periodic structure. Next, we perform Fourier transformation of $\boldsymbol{M}_s(r)$ and $l_{\rm ex}^2(r)$ for the MC to the reciprocal space using

$$M_s(r) = \sum_{\boldsymbol{G}} M_s(\boldsymbol{G})e^{i\boldsymbol{G}\cdot\boldsymbol{r}}, \tag{5}$$

$$l_{\rm ex}^2(\boldsymbol{r}) = \sum_{\boldsymbol{G}} l_{\rm ex}^2(\boldsymbol{G})e^{i\boldsymbol{G}\cdot\boldsymbol{r}}. \tag{6}$$

In PWM, we consider elliptical-shaped dots with material parameters corresponding to Py such as saturation magnetization, $M_s = 800\,{\rm kA\,m^{-1}}$, exchange constant $A = 1.3 \times 10^{-11}\,{\rm J\,m^{-1}}$, and $g = 2$, while very small values of M_s and A are assigned to the air gaps to avoid any nonphysical frequency values. A total number of 450 plane waves have been considered to ensure a satisfactory convergence of the eigenvalue problem. Here

$$M_s(\boldsymbol{G}) = \begin{cases} M_{S,A}t + M_{S,B}(1-t) & \boldsymbol{G} = 0 \\ (M_{S,A} - M_{S,B})P(\boldsymbol{G}) & \boldsymbol{G} \neq 0 \end{cases}, \tag{7}$$

where t is the filling fraction of Py in the lattice defined as $t = \frac{\pi cd}{a^2}$; c and d denote the semimajor and semiminor axis of the Py nanodots. $M_{S,A}$ and $M_{S,B}$ ($\ll M_{S,A}$) are saturation magnetizations of Py and the air gap, respectively. Finally, $P(G)$ is a function specific to the elliptical structure of the nanodots used in this calculation.

We have also used Object Orientated Micromagnetic Framework (OOMMF) software [28] for calculation of magnetic ground state of the dots under certain field configurations and Landau-Lifshitz-Gilbert (LLG) micromagnetic simulator [29] for simulation of the MFM image by discretizing the samples into cuboidal cells of dimensions $4 \times 4 \times 32\,\text{nm}^3$ (we consider the thickness of Py to be 32 nm for MFM simulation) and material parameters for Py are considered the same as that described above for PWM calculation.

III. RESULTS AND DISCUSSION

The scanning electron micrograph (SEM) of the sample is shown in Fig. 1(a), which reveals that the sample has a high quality. The dimensions of the rounded rectangles are 780 nm × 540 nm with about ±1.5% deviation in various dots in the array. The dots are tilted at an angle of $29 \pm 1^\circ$ from the x axis as shown in Fig. 1(a). The spacing between consecutive chains of dots along the z axis varies periodically between about 670 and 230 nm when moved along the x axis. The AFM image in Fig. 1(b) further reveals the topography and height of the sample. Figure 1(c) confirms that the height of the dots obtained from AFM is around 30 nm. The average roughness of the dots obtained from AFM measurement [Fig. 1(d)] is about 0.86 nm.

Figure 1(e) presents the experimental MFM image of the sample in the AC demagnetized state, which reveals the magnetic vortex state in the dots. In Fig. 1(f), we present the simulated MFM image in the AC demagnetized state, which clearly reproduces the magnetic vortex states in the dots in agreement with the experimental image. The experimental and simulated MFM images in the remanent state show a quasiuniform magnetic state, while the simulated image at $\boldsymbol{H}_3 = 330\,\text{Oe}$, obtained by raising the magnetic field from the AC demagnetized state, shows a shifted-core vortex state with the cores shifting in opposite directions for opposite spin chiralities [30]. We have simulated the static magnetic configurations of the sample at different bias magnetic field (H) values starting from the AC demagnetized state to the saturated state, i.e., $0 \leqslant \boldsymbol{H} \leqslant 500\,\text{Oe}$ at an interval of 5 Oe, and collected the snapshots of the M_y component of magnetization to form a movie (M1 in the Supplemental Material [30]). In this movie, we have shown a well controlled movement of the vortex core with the variation in H. Motion of vortex cores with opposite chiralities is reconfirmed in this movie **(M1)**. This result corresponds to a first-order phase transition from vortex to leaf state at $H = 465\,\text{Oe}$ as will be described later.

Figures 2(a)–2(g) show experimental BLS spectra, while the schematic of the BLS measurement geometry is shown in Fig. 2(h). In Figs. 2(a)–2(c), we present three representative BLS spectra for three different magnetic states, namely the leaf state ($H_1 = 850\,\text{Oe}$), the S state ($H_2 = 330\,\text{Oe}$ obtained by reducing the field from saturated state), and the shifted-core vortex state ($H_3 = 330\,\text{Oe}$ obtained by increasing the field from AC demagnetized state) at near the center of the Brillouin zone ($k \approx 0$). In Figs. 2(d)–2(f), we present three representative BLS spectra at $k = 4.1\,\text{rad}/\mu\text{m}$ (first BZ boundary, $k \approx \pi/a$) for the above three different magnetization states. We aim to study the possibility of tuning the magnonic band structure due to the interaction between the propagating SW and different spin textures as mentioned above. This is even more interesting as we could achieve two contrasting spin textures at the same bias-field magnitude of 330 Oe but having two different magnetic histories [26], namely a "field bifurcation." We observe four clear peaks for $H_1 = 850\,\text{Oe}$, while for H_2, $H_3 = 330\,\text{Oe}$, five modes are observed for $k \approx 0$ [Figs. 2(a)–2(c)]. On the contrary, at $k \approx \pi/a$, four peaks are well resolved for $H_1 = 850\,\text{Oe}$ and $H_2 = 330\,\text{Oe}$, while for $H_3 = 330\,\text{Oe}$, five well resolved peaks are observed [Figs. 2(d)–2(f)]. Interestingly, we also observe that the intensities of $F2$ and $F3$ modes have been interchanged beyond the first BZ as shown in Figs. 2(a), 2(d), and 2(g) while at the boundary of the first BZ, intensities of those two modes are nearly equal. These results correspond to a mode crossover in the wave-vector domain.

The experimental SW dispersion relations for these three different bias fields are plotted in Figs. 3(a)–3(c) as symbols. While for $H_1 = 850\,\text{Oe}$ three clear band gaps (BGs) of 0.53 GHz (between $F1$ and $F2$), 1.00 GHz (between $F2$ and $F3$) and 3.5 GHz (between $F3$ and $F4$) are observed, H_2, $H_3 = 330\,\text{Oe}$ show starkly different behavior. For $H_2 = 330\,\text{Oe}$, the two lowest frequency bands merge at the first BZ boundary leaving only two BGs between $F1$, $F1'$, and $F2$ (1.05 GHz), $F2$, and $F3$ (1.12 GHz). On the contrary for $H_3 = 330$, three BGs of 0.8 GHz ($F1$ and $F1'$), 1.26 GHz ($F1'$ and $F2$), and 2.02 GHz ($F2$ and $F3$) are observed. The calculated magnonic band structures using PWM are shown in Figs. 3(a) and 3(b) as the three-dimensional surface plots superposed on the experimental dispersions. The color map (white to blue) of the intensity of SW modes [$I \propto |m_y(k)|^2$] is shown next to the dispersion. The color scale of the surface plot is adjusted such that only the high-intensity SWs are visible as blue regions, which clearly reveals that the high-intensity experimental and calculated modes are in general agreement.

It is clear that the internal spin texture modulates the SW propagation significantly, which has also been shown in different systems before [31,32]. However, the observation of different spin textures and the ensuing difference in magnon dispersion and magnon BG at an identical magnetic field, the field-bifurcation phenomenon [26] in dynamic systems, may open up applications in spintronics and magnonics. In order to understand the spin-texture-dependent magnon dispersion, we first calculate the SW mode profiles for $H_1 = 850\,\text{Oe}$ (the ground state shows the leaf state) and $H_2 = 330\,\text{Oe}$ (the ground state shows the S state), as shown in Fig. 4.

In the following, we will use SW mode quantization numbers such as (m, n), which describe the quantization along the major and the minor axes of the dots. Figure 4 reveals that at the center of the BZ, $F1$ is a propagating SW mode extending through a channel joining the dots in both leaf and S states leading towards almost identical dispersion in both states. However, an additional mode $F1'$ appears in the S state, which also propagates through the same channel but

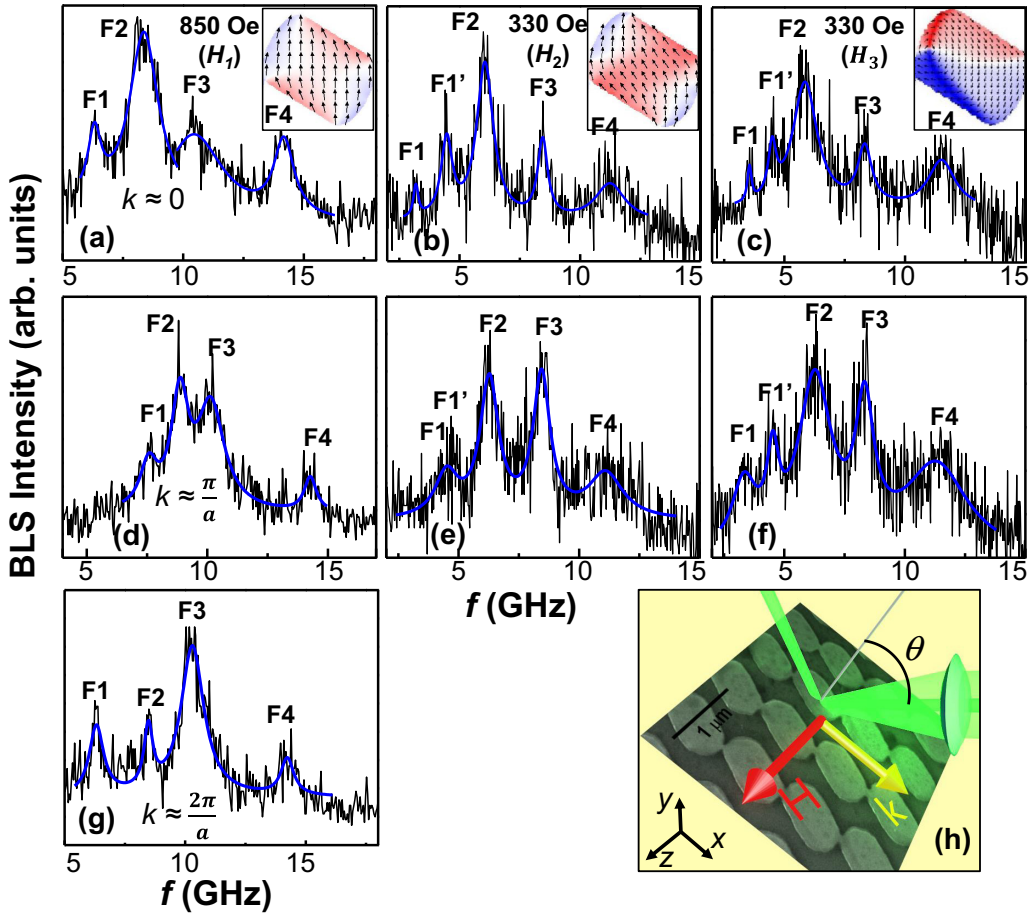

FIG. 2. (a)–(c) The Stokes side of BLS spectra taken at three different magnetic history, i.e., leaf state ($H_1 = 850$ Oe), S state ($H_2 = 330$ Oe, when decreased from saturation field), and shifted-core vortex state ($H_3 = 330$ Oe, when increased from AC demagnetized state) at $k \approx 0$. The simulated magnetic states are shown in the insets. (d)–(f) The Stokes side of BLS spectra taken for leaf, S and shifted-core vortex state, respectively, at the first BZ boundary ($k \approx \pi/a$). (g) The Stokes side of BLS spectra taken for the leaf state at the second BZ boundary ($k \approx 2\pi/a$). The solid lines represent the Lorentzian fits to identify the peaks. (h) Schematic of BLS measurement in the Damon-Eshbach (DE) geometry.

having additional quantization (3,1) and a weakly dispersive nature. At the boundary of the first BZ, $F1$ ceases to propagate through the channel, showing a pseudoextended nature between two successive dots with quantization numbers (4,1). Mode $F2$ shows qualitatively similar dispersion for both leaf and S states, while the dispersion is steeper in the leaf state indicating greater group velocity. Interestingly, the mode profiles vary significantly and the mode quantization axis

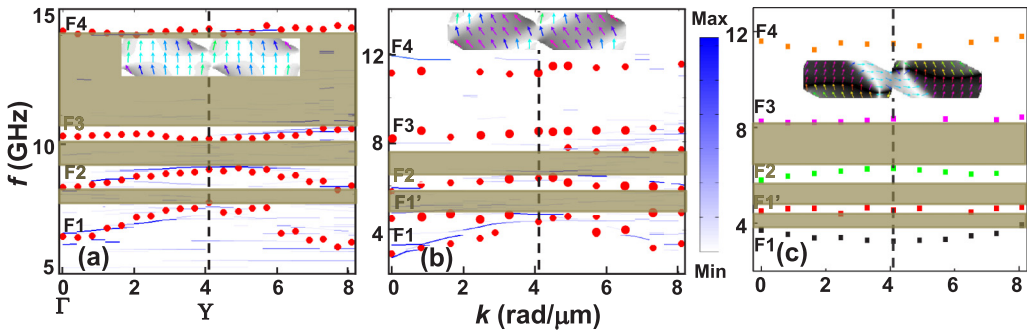

FIG. 3. (a)–(c) Magnonic band structure corresponding to three different magnetic states, i.e., leaf, S and shifted-core vortex state, respectively. Here, filled symbols represent BLS peak frequencies for different k values, the dashed vertical line is the boundary of the first BZ, while the band gap is shown by the shaded areas. The three-dimensional surface plots of the plane-wave method calculated spin-wave dispersion is superposed on the experimental data in (a) and (b). The corresponding color map for (a) and (b) is shown at the right side of the figure. The simulated magnetization configuration in the spin-wave propagation channels for the three magnetic states are shown in the insets.

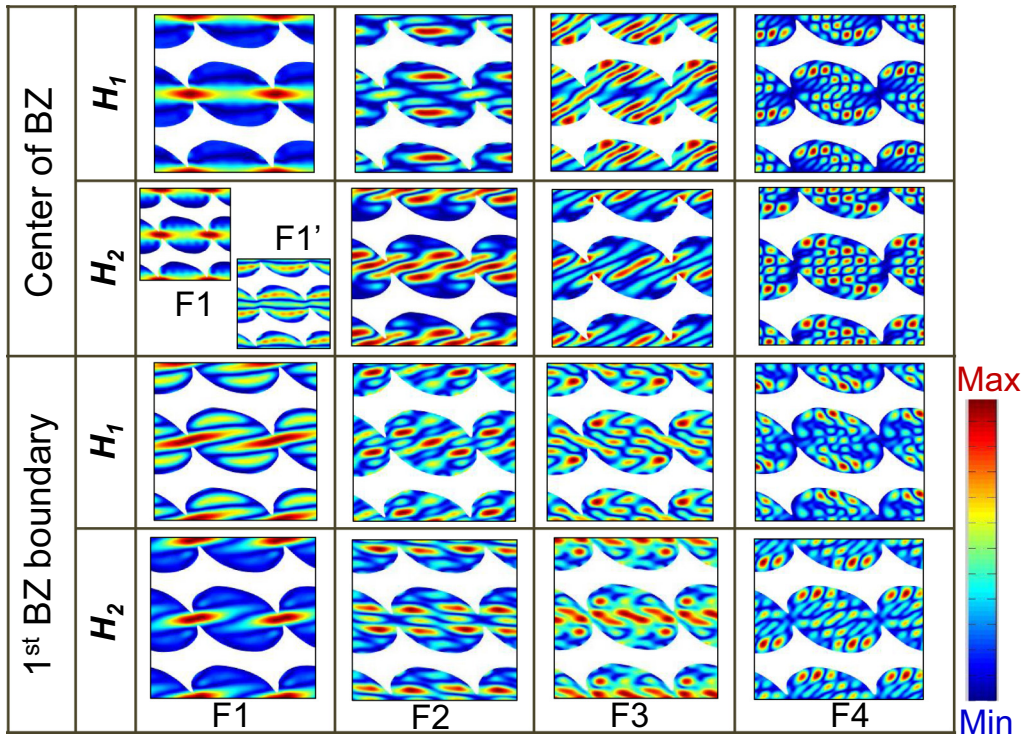

FIG. 4. Spatial profiles of selected spin-wave modes ($F1$, $F1'$, $F2$, $F3$, and $F4$) for two different magnetic states, namely the leaf and S state at $k \approx 0$ and $k \approx \pi/a$.

rotates by 24° in the S state with (m, n) as (4,2) and (6,1) in the leaf and S state. At the first BZ, both the quantization numbers and axes change to (7,1), 19° in the leaf state and (5,2), 0° in the S state. The mode $F3$ shows a negative dispersion in the leaf state, while it is almost dispersionless in the S state. This is evident from the mode profile at the center of the BZ, which shows pseudoextended character in the leaf state with mode quantization numbers (8,2), allowing transfer of energy through the chain of dots. However, the mode is fully localized within the individual dots in the S state with quantization numbers (7,2) leading towards no or negligible transfer of energy. At the edge of the first BZ, the mode quantization number becomes (2,4) and (3,4) and quantization axes change by 160° in the leaf and S state, respectively. Mode $F4$ is dispersionless in both states, showing fully localized behavior with quantization numbers (10,8) and (9,5) in the leaf and S states at the center of the BZ. These modes transform into (9,6) and (11,6) at the boundary of the first BZ.

Next, we inspect the detailed spin textures within the channels of propagation through the chains of dots for all three magnetization states, namely, leaf, S, and vortex states as shown in the insets of Figs. 3(a)–3(c). In the leaf state the spins are almost parallel with slight periodic canting within the channel of SW propagation and hence the SW dispersion is affected primarily by the periodicity of the structure. In the S state the SW interacts with a spin texture with sharp contrast posing additional periodicity in the magnetic potential. The ensuing scattering of the SWs from these additional scattering centers probably leads to the new SW mode $F1'$. On the contrary the spin texture in the shifted-core vortex state shows the formation of 90° domains near the connected regions and this is the origin of the drastically different magnonic band structure in this case. The weakly negative dispersion of $F1$ is probably associated with this spin texture. Due to the technical difficulties, PWM calculations could not be performed in the shifted-core vortex state. However, to extract the information about the SW mode profiles in this magnetic state, we have used OOMMF micromagnetic simulation when the connected dots are uniformly excited at $k = 0$ and a home-built code [33]. The results are shown in Fig. 5(a). All the modes show nonuniform character with $F1$ showing a somewhat extended nature with its power flowing through the nanochannels connecting the dots. Consequently, this mode shows a dispersive nature. $F1'$ shows almost nonexistent power in the nanochannels and consequently this mode does not extend throughout the sample showing a nondispersive character. $F2$ again shows a weakly extended nature and hence a weak dispersion in the magnonic band structure. $F3$ and $F4$ are fully quantized modes localized in the individual dots with negligible power in the propagation channel and they are fully dispersionless. This causes the nature of dispersion of the SWs observed in this case.

We now look into the transformation between the above three magnetic states. The calculated M-H curves in Fig. 5(b) clearly show that the transformation from the leaf to the S state occurs continuously as we reduce the magnetic field from the saturation state to lower value. On the contrary, when the magnetic field is increased from the AC demagnetized state, the magnetization shows a sudden jump due a first-order phase transition at around 465 Oe (vortex annihilation field) as the vortex state is transformed into the leaf state. This is also reflected into the calculated SW frequency as shown in the inset of Fig. 5(b). The SW frequency decreases monotonically as the field is reduced from the saturation and

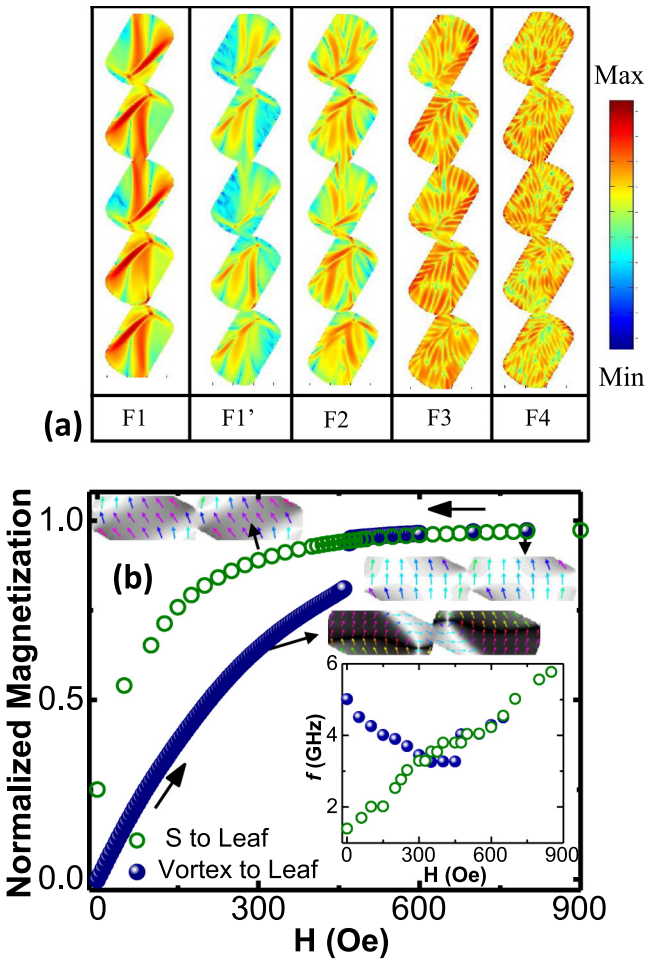

FIG. 5. (a) Simulated power maps showing spin-wave modes ($F1$, $F1'$, $F2$, $F3$, and $F4$) profile for the shifted-core vortex state at $k = 0$. The corresponding color map is shown at the right side of the figure. (b) Simulated variation of normalized magnetization with applied magnetic field. Arrows represent the path of variation from one spin texture to another spin texture. Inset represents simulated spin-wave frequency vs bias magnetic field along two different paths of magnetic field history.

the magnetization state transforms from the leaf to S state. On the contrary, the frequency shows a clear jump at a magnetic field of about 465 Oe, followed by a minimum and an increase as the field is further reduced. Such a minimum in frequency vs magnetic field indicates a SW mode softening as observed before [34,35]. The observed variation in the spin texture and its ensuing magnetic properties leads to only a quantitative change in the SW dispersion in the leaf and the S state but a major qualitative variation in the dispersion of the mode $F1$ where a negative dispersion in the shifted-core vortex state is observed as opposed to a positive dispersion in both the leaf and the S states.

IV. CONCLUSIONS

In summary, we have performed a combined experimental and numerical study of magnonic band structure in coupled rectangular-shaped ferromagnetic dots with rounded edges. By varying the magnetic field strength and history, we were able to obtain three different spin textures, namely the S state, the leaf state, and the shifted-core vortex state. The magnonic band structure exhibited a remarkable variation due to the interaction of SW with different spin textures, viz. the variation in number of modes and their dispersion behavior. This is particularly prominent when the spin textures provide abrupt variation in the propagation channel of the SWs, namely by S state and shifted-core vortex state, where an additional mode appears. The results are reproduced by plane-wave method-based numerical calculations. The calculated SW mode profiles show a remarkable variation of power in the propagation channel, quantization number of the modes, and their quantization axes originating from different spin textures in the ground state. Further calculation shows a first-order phase transition in the magnetization as well as frequency with bias field strength for the transformation from vortex to leaf state, and a continuous change from S to leaf state. Such a rich variation in the static and dynamic magnetic characteristics lead to the ensuing variation in magnonic band structures. Observation of such reconfigurable band structure with external bias magnetic field and ensuing spin texture would pave the way for the advancement of a new research field called topological magnonics.

ACKNOWLEDGMENTS

A.B. gratefully acknowledges the financial assistance from the S. N. Bose National Centre for Basic Sciences under Project No. SNB/AB/18-19/211. S.B. acknowledges Science and Engineering Research Board, DST, India, under Grant No. CRG/2018/002080 for funding. A.K.M., A.A., C.B., and S.C. acknowledge S. N. Bose National Centre for Basic Sciences for a research fellowship, A.K.C. acknowledges DST INSPIRE, and J.S. acknowledges DST, Government of India.

[1] K. Molvig, M. S. Tekula, and A. Bers, Phys. Rev. Lett. **38**, 1404 (1977).
[2] I. Žutić, J. Fabian, and S. Das Sarma, Rev. Mod. Phys. **76**, 323 (2004).
[3] S. D. Bader and S. S. P. Parkin, Annu. Rev. Condens. Matter Phys. **1**, 71 (2010).
[4] S. A. Nikitov, P. Tailhades, and C. S. Tsai, J. Magn. Magn. Mater. **236**, 320 (2001).
[5] V. V. Kruglyak, S. O. Demokritov, and D. Grundler, J. Phys. D: Appl. Phys. **43**, 260301 (2010).
[6] A. Manchon, J. Železný, I. M. Miron, T. Jungwirth, J. Sinova, A. Thiaville, K. Garello, and P. Gambardella, Rev. Mod. Phys. **91**, 035004 (2019).
[7] A. V. Chumak, V. I. Vasyuchka, A. A. Serga, and B. Hillebrands, Nat. Phys. **11**, 453 (2015).

[8] B. K. Mahato, B. Rana, D. Kumar, S. Barman, S. Sugimoto, Y. Otani, and A. Barman, Appl. Phys. Lett. **105**, 012406 (2014).
[9] Z. K. Wang, V. L. Zhang, H. S. Lim, S. C. Ng, M. H. Kuok, S. Jain, and A. O. Adeyeye, ACS Nano **4**, 643 (2010).
[10] R. Mandal, S. Saha, D. Kumar, S. Barman, S. Pal, K. Das, A. K. Raychaudhuri, Y. Fukuma, Y. Otani, and A. Barman, ACS Nano **6**, 3397 (2012).
[11] S. Saha, R. Mandal, S. Barman, D. Kumar, B. Rana, Y. Fukuma, S. Sugimoto, Y. Otani, and A. Barman, Adv. Funct. Mater. **23**, 2378 (2013).
[12] S. Tacchi, G. Duerr, J. W. Klos, M. Madami, S. Neusser, G. Gubbiotti, G. Carlotti, M. Krawczyk, and D. Grundler, Phys. Rev. Lett. **109**, 137202 (2012).
[13] C. Banerjee, S. Choudhury, J. Sinha, and A. Barman, Phys. Rev. Appl. **8**, 014036 (2017).
[14] S. Barman, A. Barman, and Y. Otani, IEEE Trans. Mag. **46**, 1342 (2010).
[15] A. Vogel, M. Martens, M. Weigand, and G. Meier, Appl. Phys. Lett. **99**, 042506 (2011).
[16] S. Barman, A. Barman, and Y. Otani, J. Phys. D: Appl. Phys. **43**, 335001 (2010).
[17] D. Bhowmik, L. You, and S. Salahuddin, Nat. Nanotechnol. **9**, 59 (2013).
[18] D. B. Carlton, N. C. Emley, E. Tuchfeld, and J. Bokor, Nano Lett. **8**, 4173 (2008).
[19] A. Imre, G. Csaba, L. Ji, A. Orlov, G. H. Bernstein, and W. Porod, Science **311**, 205 (2006).
[20] H. Jung, Y.-S. Choi, K.-S. Lee, D.-S. Han, Y.-S. Yu, M.-Y. Im, P. Fischer, and S.-K. Kim, ACS Nano **6**, 3712 (2012).
[21] D. Kumar, S. Barman, and A. Barman, Sci. Rep. **4**, 4108 (2014).
[22] S. Saha, S. Barman, J. Ding, A. O. Adeyeye, and A. Barman, Appl. Phys. Lett. **103**, 242416 (2013).
[23] A. Haldar, D. Kumar, and A. O. Adeyeye, Nat. Nanotechnol. **11**, 437 (2016).
[24] M. Giglio, S. Musazzi, and U. Perini, Phys. Rev. Lett. **47**, 243 (1981).
[25] S. H. Strogatz, *Nonlinear Dynamics and Chaos with Applications to Physics, Biology, Chemistry, and Engineering* (Perseus Books Publishing, L.L.C., Reading, Massachusetts, 1994).
[26] R. P. Cowburn, D. K. Koltsov, A. O. Adeyeye, M. E. Welland, and D. M. Tricker, Phys. Rev. Lett. **83**, 1042 (1999).
[27] M. Krawczyk and H. Puszkarski, Phys. Rev. B **77**, 054437 (2008).
[28] M. Donahue and D. G. Porter, OOMMF User's Guide, Version 1.0, NIST Interagency Report No. 6376 (National Institute of Standard and Technology Gaithersburg, MD, 1999).
[29] M. R. Scheinfein and A. Price, *LLG User Manual* v2.50, http://llgmicro.home.mindspring.com, 2003.
[30] See Supplemental Material at http://link.aps.org/supplemental/10.1103/PhysRevB.101.224426 for additional experimental and simulated MFM images and a simulated movie (M1) for vortex core motion in the sample with magnetic field.
[31] K. Wagner, A. Kákay, K. Schultheiss, A. Henschke, T. Sebastian, and H. Schultheiss, Nat. Nanotechnol. **11**, 432 (2016).
[32] F. Garcia-Sanchez, P. Borys, R. Soucaille, J.-P. Adam, R. L. Stamps, and J.-V. Kim, Phys. Rev. Lett. **114**, 247206 (2015).
[33] D. Kumar, O. Dmytriiev, S. Ponraj, and A. Barman, J. Phys. D: Appl. Phys. **45**, 015001 (2011).
[34] K. Adhikari, S. Sahoo, A. K. Mondal, Y. Otani, and A. Barman, Phys. Rev. B **101**, 054406 (2020).
[35] K. Adhikari, S. Barman, R. Mandal, Y. Otani, and A. Barman, Phys. Rev. Appl. **10**, 044010 (2018).